AIAA JOURNAL
Vol. 39, No. 8, August 2001

Unsteady Flow Evolution in Porous Chamber with Surface Mass Injection, Part 1: Free Oscillation

Sourabh Apte* and Vigor Yang†
Pennsylvania State University, University Park, Pennsylvania 16802

Unsteady flow evolution in a porous chamber with surface mass injection simulating a nozzleless rocket motor has been investigated numerically. The analysis is based on a large-eddy-simulation technique in which the spatially filtered and Favre averaged conservation equations for large, energy-carrying turbulent structures are solved explicitly. The effect of the unresolved scales is modeled semi-empirically by considering adequate dissipation rates for the energy present in the resolved scale motions. The flowfield is basically governed by the balance between the inertia force and pressure gradient, as opposed to viscous effects and pressure gradient corresponding to channel flows without transpiration. It accelerates from zero at the head end and becomes supersonic in the divergent section of the nozzle. Three successive regimes of development, laminar, transitional, and fully turbulent flow, are observed. Transition to turbulence occurs away from the porous wall in the midsection of the motor, and the peak in the turbulence intensity moves closer to the wall farther downstream as the local Reynolds number increases. Increase in pseudoturbulence level at the injection surface causes early transition to turbulence. As the flow develops farther downstream, the velocity profile transits into the shape of a fully developed turbulent pipe flow with surface transpiration. The compressibility effect also plays an important role, causing transition of the mean velocity profiles from their incompressible flow counterparts as the local Mach number increases. The flow evolution is characterized primarily by three nondimensional numbers: injection Reynolds number, centerline Reynolds number, and momentum flux coefficient.

Nomenclature

A = chamber cross section
c = speed of sound
c_S = Smagorinsky constant
D = near-wall damping function
E = turbulence energy
$\tilde{e}$ = filtered total specific energy
f = frequency, Hz
G = spatial filter function
$G_{k,u}$ = amplification factor per time step
h = chamber half-height, m
$\tilde{h}$ = total specific enthalpy
I = turbulence intensity, $\sqrt{(\overline{u'u'} + \overline{v'v'})}$
I_τ = number of time steps required for one eddy lifetime
k = wave number, 1/m
L = chamber length, m
ℓ = turbulence length scale, m
$\dot{m}$ = injection mass flux, kg/m^{2}s
M = mean Mach number averaged over given cross section
M_c = mean Mach number at centerline
Pr = Prandtl number
p = pressure, Pa
q = large-scale velocity, m/s
$\Re$ = random number generator
Re = Reynolds number
S_{ij} = strain-rate tensor, $[(\partial u_i/\partial x_j) + (\partial u_j/\partial x_i)]/2 - \delta_{ij}(\partial u_k/\partial x_k)/3$
Sr = Strouhal number, fh/v_w
T = temperature, K
t = time, s
u = axial velocity, m/s
u_τ = friction velocity, $\sqrt{(\tau_w/\rho)}$, m/s
v = vertical velocity, m/s
v_w = injection velocity at wall, m/s
γ = ratio of specific heats
Δ = filter width
δ = constant ≈ 0.0025
δ_{ij} = Kronecker delta
ε_p = pseudoturbulence level
ε_v = artificial dissipation coefficient
η = Kolmogorov length scale, m
κ = thermal conductivity, W/mK
μ = dynamic viscosity, kg/ms
ν = kinematic viscosity, m^2/s
ν_s = subgrid-scale kinematic viscosity, m^2/s
ξ = grid parameter for large-eddy simulation
ρ = density, kg/m^3
σ = Courant–Friedrichs–Lewy number
τ = viscous shear stress, N/m^2

Subscripts

b = bulk mean quantity
c = centerline
w = wall

Superscripts

r = resolved-scale component
s = subgrid-scale component
$\sim$ = density-weighted quantity
$-$ = time-averaged quantity
$'$ = fluctuating component due to turbulence

Received 10 October 2000; revision received 8 February 2001; accepted for publication 14 February 2001.

*Ph.D. Student, Department of Mechanical Engineering.
†Professor, Department of Mechanical Engineering; vigor@psu.edu. Associate Fellow AIAA.

I. Introduction

THE present work attempts to explore the development of the internal flowfield in a porous chamber with surface transpiration, as shown schematically in Fig. 1. The term "transpiration" is used collectively to refer to injection or blowing through porous surfaces. Wall-bounded turbulent flows with surface transpiration have been of great interest since the early 1950s, when blowing was first investigated as means of cooling aerodynamic surfaces under high-velocity flight conditions. Film-cooling techniques commonly used in cooling gas-turbine blades resemble transpired boundary layers. The transpired fluid absorbs thermal energy from the porous surface and reduces heat transfer rates substantially. Mass transfer

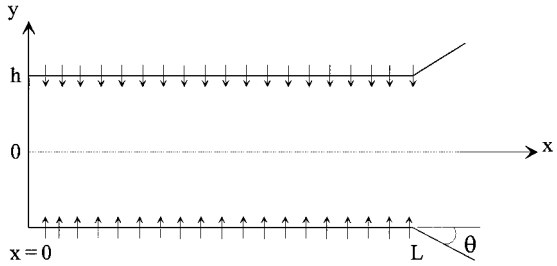

Fig. 1 Schematic diagram of porous chamber with surface mass injection simulating nozzleless rocket motor.

and diffusion problems involving evaporation or sublimation from (or condensation onto) the porous wall necessitate modeling of flow with transpiration. Suction is used as a means to control and delay transition to turbulence in flow over an airfoil. The effect of transpiration on the flow development in a boundary layer is also found to be significant: When fluid is injected, the boundary layer becomes thicker, the skin friction decreases, and turbulent fluctuations are enhanced. Transpiration greatly alters the wall-layer dynamics and the conventional law of the wall fails to predict the wall stresses accurately. Direct applications of flow with transpiration in filtration and diffuse separation of gaseous isotopes have been reported in the literature. Combustion-induced flowfields in solid-propellant rocket motors can be thought of as mass injection from the burning surface. Fully developed stationary flowfields subjected to time-dependent, periodic unsteadiness are of utmost importance in analyzing the unstable motions in rocket propulsion systems. The wide range of engineering applications necessitates in-depth analysis of boundary layers under the influence of surface transpiration.

Extensive experimental work on flows with surface transpiration was carried out at the Massachusetts Institute of Technology by Mickley et al.[1] Between 1967 and 1975 many experiments were carried out at Stanford to study the characteristics of transpiration on boundary layers. Simpson et al.,[2] Julien et al.,[3] and many others made extensive measurements of mean velocity profiles, skin-friction coefficients, and Reynolds stresses in transpired boundary layers over a flat plate. A comprehensive review of experiments and other studies on transpiration can be obtained by Kays[4] and Kays and Crawford.[5] Recently, the large-eddy-simulation (LES) technique was used by Piomelli et al.[6] to study the effects of transpiration on turbulent channel flows. Considerable improvement in predicting the wall-layer and turbulence characteristics was achieved. Sumitani and Kasagi[7] performed direct numerical simulations (DNS) of flow through porous channels with blowing from one side and suction through the opposite wall at low transpiration rates ($v_w/u_\tau \sim 0.05$). Results indicated that mass injection decreases the friction coefficient, but tends to stimulate the near-wall turbulence activity so that the Reynolds stresses and turbulent heat fluxes are increased, whereas suction has an inverse influence.

Flow evolution in a porous chamber with surface mass injection resembles the flowfield ensuing from the burning of solid propellant in a rocket motor. An analytical description of the inviscid, rotational laminar flowfield in such a configuration was first obtained by Taylor[8] and later validated by Culick.[9] Beddini[10] investigated the development of turbulent flowfields through porous-walled ducts at large injection Reynolds numbers, indicating three different flow regimes. The velocity field develops in accordance with laminar flow theory near the head end and undergoes transition in the midsection of the chamber. Transition of the mean axial velocity profiles occurs farther downstream in the fully developed turbulent flowfield. These results were further validated by Traineau et al.[11] through their experimental study on a nozzleless rocket motor at high injection Reynolds number (15×10^3) and Mach number (0.0095). The effect of compressibility on transition of the mean velocity profiles from their incompressible counterparts was elucidated in detail. A theoretical analysis of inviscid but rotational and compressible flowfield in a porous duct with varying injection rates and favorable pressure gradients was carried out by Balakrishnan et al.[12] They explored the effects of compressibility in flattening the radial profiles of axial velocity in a manner analogous to that arising from turbulence in flows without injection. An experimental study of the flowfield in a porous chamber was carried out by Dunlap et al.[13] at low injection Mach numbers (0.0018 and 0.0036), with turbulence properties measured at various locations. The corresponding injection Reynolds numbers (9×10^3 and 18×10^3) were typical of rocket motor conditions.

Several numerical simulations have been performed to study the flowfield within a rocket combustion chamber. Sabnis et al.[14] and Tseng[15] used conventional single-point turbulence closure schemes and obtained good comparison of the mean flowfield with experimental data, but overpredicted the turbulence intensity levels within the chamber. Nicoud et al.[16] performed DNS at high injection rates ($v_w/u_\tau \sim 1.4$) in an attempt to reproduce flow conditions representative of a solid rocket motor to study the effect of high blowing rate on the wall layer. Ciucci et al.[17] conducted a detailed comparison of DNS results with standard $k-\varepsilon$ turbulence closure schemes and the $\overline{v^2}-f$ model utilizing the velocity component normal to the streamlines, $\overline{v^2}$, and transport equation for f, representing the production of $\overline{v^2}$. They pointed out that the appropriate velocity scale for turbulent transport near the wall is $\overline{v^2}$ instead of the turbulence intensity and showed considerable improvement over standard $k-\varepsilon$ models.

In an effort to characterize unsteady motions in rocket motors, several numerical analyses based on LES of nonreacting flows have been performed. Lupoglazoff and Vuillot[18] studied the vortex-shedding phenomenon in injection driven flows and compared the pressure fluctuation levels with their experimental results. The hydrodynamic instabilities in the flow drive pressure fluctuations within the chamber. Liou and Lien,[19] Liou et al.,[20] and Apte and Yang[21] conducted two-dimensional time-resolved simulations of flows through nozzleless rocket motors at very high injection rates ($v_w/u_\tau \sim 1.5-6$) to achieve better comparison of turbulence intensity and axial velocity profiles as compared with the second-order turbulence closures. Their simulations indicated that the injection velocity increases farther downstream because of high-density gradients in the axial direction near the throat. Apte and Yang[22] also performed LES of internal flow development in a three-dimensional rectangular rocket motor to obtain better predictions of turbulence properties and explored the physical aspects of the unsteady flow evolution in detail. The present work represents significant progress on simulating the internal flowfield in a porous chamber with surface mass injection. This study will provide a basis from which the effect of forced acoustic excitations on the mean and turbulent flowfields can be further explored.[23]

The present study starts with time-resolved simulations of the motor internal flowfield in a stationary turbulent environment. In the following sections, a theoretical formulation with turbulence modeling is summarized, and the boundary conditions and their implementation are described. A priori estimation of the spatial and temporal resolution required to capture the flow motions accurately within the chamber is performed based on a detailed stability analysis of the numerical scheme. The main objectives of this work are 1) to explore the turbulence transition and flow evolution in a porous chamber with surface mass injection at high Reynolds and Mach numbers, 2) to assess the accuracy of the present simulations, and 3) to form a basis to study the energy exchange mechanisms among the mean, periodic, and turbulent flowfields by imposing periodic excitations in the stationary flowfield.

II. Theoretical Formulation

Figure 1 shows the physical model of concern, a rectangular porous chamber with surface mass injection. The configuration simulates the flow development in a nozzleless solid-propellant rocket motor studied experimentally by Traineau et al.[11] The chamber is closed at the head end and is connected downstream with a choked divergent nozzle at the exit. Air is injected uniformly through the porous wall at constant pressure and mass flow rate. The flow accelerates from zero at the head end and becomes supersonic in the nozzle section.

Governing Equations

The flowfield is governed by the following conservation equations of mass, momentum and energy,[24]

$$\frac{\partial \rho}{\partial t} + \frac{\partial (\rho u_k)}{\partial x_k} = 0 \tag{1}$$

$$\frac{\partial (\rho u_k)}{\partial t} + \frac{\partial (\rho u_k u_l)}{\partial x_l} = -\frac{\partial p}{\partial x_k} + \frac{\partial \sigma_{kl}}{\partial x_l} \tag{2}$$

$$\frac{\partial (\rho e)}{\partial t} + \frac{\partial (\rho \tilde{h} u_k)}{\partial x_k} = -\frac{\partial q_k}{\partial x_k} + \phi \tag{3}$$

where u is the velocity vector, p the thermodynamic pressure, and e the total specific internal energy. The standard tensor notation with repeated indices implying summation over the axial and vertical components is used. The viscous stress σ_{kl}, the thermal diffusion q_k, and the viscous dissipation ϕ are defined as

$$\sigma_{kl} = -\frac{2}{3}\mu \frac{\partial u_j}{\partial x_j}\delta_{kl} + \mu\left(\frac{\partial u_k}{\partial x_l} + \frac{\partial u_l}{\partial x_k}\right) \tag{4}$$

$$q_k = -k\frac{\partial T}{\partial x_k} \tag{5}$$

$$\phi = -\frac{2}{3}\mu\left(\frac{\partial u_k}{\partial x_k}\right)^2 + \mu\left(\frac{\partial u_k}{\partial x_l} + \frac{\partial u_l}{\partial x_k}\right)\frac{\partial u_k}{\partial x_l} \tag{6}$$

where k is the thermal conductivity. The governing equations are supplemented with the equation of state for an ideal gas,

$$p = \rho R T \tag{7}$$

where R is the gas constant. The thermodynamic properties are assumed constant for the present case because the temperature variation within the flowfield of interest is not significant.

Turbulence closure is obtained based on the LES technique, in which large, energy-carrying structures are computed explicitly and the effect of small-scale motions on the resolved scales is modeled. A spatial filter G is used to decompose the flow variables into large (resolved) and subgrid (unresolved) scales[25]:

$$\mathfrak{J}(\boldsymbol{x}, t) = \mathfrak{J}^r(\boldsymbol{x}, t) + \mathfrak{J}^s(\boldsymbol{x}, t) \qquad \text{with}$$

$$\mathfrak{J}^r(\boldsymbol{x}, t) = \int_D G(\boldsymbol{x} - \boldsymbol{x}', \Delta)\mathfrak{J}(\boldsymbol{x}', t)\, \mathrm{d}^3\boldsymbol{x}' \tag{8}$$

where D is the entire domain, Δ the computational mesh size that determines the size and structure of the unresolved scales, and $\mathfrak{J}$ any flow property, namely, ρ, p, u_i, or T. The superscripts r and s represent the resolved and unresolved scales of flow properties. The Favre averaging is further used to simplify the governing equations for compressible flows.[25] This density-weighted averaging eliminates complex triple correlations between density and velocity fluctuations in the governing equations and is given as

$$\tilde{\mathfrak{J}}^r = (\rho \mathfrak{J})^r / \rho^r \tag{9}$$

Contrary to the more traditional Favre averaging,[26]

$$\tilde{\bar{\mathfrak{J}}}^r \neq \tilde{\mathfrak{J}}^r, \qquad \tilde{\mathfrak{J}}^s \neq 0 \tag{10}$$

The filtered form of the governing equations can be written as

$$\frac{\partial \rho^r}{\partial t} + \frac{\partial \left(\rho^r \tilde{u}_k^r\right)}{\partial x_k} = 0 \tag{11}$$

$$\frac{\partial \left(\rho^r \tilde{u}_k^r\right)}{\partial t} + \frac{\partial \left(\rho^r \tilde{u}_k^r \tilde{u}_l^r\right)}{\partial x_l} = -\frac{\partial p^r}{\partial x_k} + \frac{\partial \sigma_{kl}^r}{\partial x_l} + \frac{\partial \tau_{kl}}{\partial x_l} \tag{12}$$

$$\frac{\partial (\rho^r \tilde{e}^r)}{\partial t} + \frac{\partial \left(\rho^r \tilde{h}^r \tilde{u}_k^r\right)}{\partial x_k} = -\frac{\partial q_k^r}{\partial x_k} - \frac{\partial Q_k}{\partial x_k} - \frac{\partial \left(\rho^r \overline{\overline{\tilde{u}_l^r \tilde{u}_l^r \tilde{u}_k^r}}\right)}{\partial x_k} + \phi^r \tag{13}$$

where $p^r = \rho^r R \tilde{T}^r$ and $\bar{\bar{(\,)}}$ represents the filtering operation defined by Eq. (8) and σ_{kl}^r and ϕ^r are the viscous stresses and dissipation of the resolved scales, respectively. The terms τ_{kl} and Q_k are the subgrid-scale (SGS) stresses and heat fluxes, respectively, and are given as

$$\tau_{kl} = -\rho^r\left(\left(\overline{\overline{\tilde{u}_k^r \tilde{u}_l^r}} - \overline{\overline{\tilde{u}_k^r}}\,\overline{\overline{\tilde{u}_l^r}}\right) + \left(\overline{\overline{u_k^s \tilde{u}_l^r}} + \overline{\overline{\tilde{u}_k^r u_l^s}} - \overline{\overline{\tilde{u}_k^r}}\,\tilde{u}_l^s - \tilde{u}_k^s\,\overline{\overline{\tilde{u}_l^r}}\right) + \left(\overline{\overline{u_k^s u_l^s}} - \tilde{u}_k^s \tilde{u}_l^s\right)\right) \tag{14}$$

$$Q_k = C_p \rho^r\left(\left(\overline{\overline{\tilde{u}_k^r \tilde{T}^r}} - \overline{\overline{\tilde{u}_k^r}}\,\overline{\overline{\tilde{T}^r}}\right) + \left(\overline{\overline{u_k^s \tilde{T}^r}} + \overline{\overline{\tilde{u}_k^r \tilde{T}^s}} - \overline{\overline{\tilde{u}_k^r}}\,\tilde{T}^s - \tilde{u}_k^s\,\overline{\overline{\tilde{T}^r}}\right) + \left(\overline{\overline{u_k^s T^s}} - \tilde{u}_k^s \tilde{T}^s\right)\right) \tag{15}$$

The first terms in the parentheses in Eqs. (14) and (15) can be computed directly once a filter function is defined. The other terms need to be modeled and represent the effect of unresolved scales on resolved scales of motion. One important feature of any SGS model is to provide adequate energy flux. Here, flux means transport of energy from resolved scales to unresolved SGS, and the rate of dissipation represents the flux of energy through the inertial subrange of the turbulence spectrum.[27] A Smagorinsky model extended to compressible flows is used to treat these terms, as suggested by Erlebacher et al.[25] Accordingly, the SGS terms are modeled by relating the SGS stresses to the large-scale strain-rate tensor S_{kl}^r, through the eddy viscosity ν_T and the SGS kinetic energy K, as follows:

$$\tau_{kl} = 2\nu_T \rho^r S_{kl}^r - \frac{2}{3}\delta_{kl} K \tag{16}$$

$$S_{kl}^r = \frac{1}{2}\left(\frac{\partial \tilde{u}_k^r}{\partial x_l} + \frac{\partial \tilde{u}_l^r}{\partial x_k}\right) - \frac{1}{3}\delta_{kl}\left(\frac{\partial \tilde{u}_i^r}{\partial x_i}\right) \tag{17}$$

with

$$\nu_T = c_D (D\Delta)^2 \left(2S_{ij}^r S_{ij}^r\right)^{\frac{1}{2}}, \qquad K = c_I \rho^r (D\Delta)^2 \left(2S_{ij}^r S_{ij}^r\right) \tag{18}$$

where Δ is the average size of the computational cell and $c_D (\approx 0.01)$ and $c_I (\approx 0.007)$ are the model constants, based on the work of Erlebacher et al.[25] The Van Driest damping function D is used to take into account the inhomogeneities near the surface (see Ref. 20), and is expressed as

$$D = 1 - \exp[1 - (y^+)^3/26^3] \tag{19}$$

where $y^+ = y\tilde{u}_\tau^r/\nu$. The effect of surface transpiration is indirectly obtained through the wall shear stress τ_w^r, which appears in the computation of the friction velocity $\tilde{u}_\tau^r$. The heat flux is modeled similarly by defining an eddy diffusivity and relating it to the viscosity through the turbulent Prandtl number Pr_T:

$$Q_k = -\rho^r C_p \frac{\nu_T}{Pr_T}\frac{\partial \tilde{T}^r}{\partial x_k} \tag{20}$$

A standard value of 0.7 is used for the turbulent Prandtl number based on air as the medium.[25]

Boundary Conditions

The method of characteristics is used to specify the boundary conditions. For the subsonic inflow through the porous surface, three conditions need to be specified. The mass and energy fluxes are kept constant, and the injection velocity is assumed to be vertical, that is, $\tilde{u}^r = 0$. The effect of surface roughness and pseudoturbulence level at the porous surface is considered by imposing white noise in the mass flow rate. The level of pseudoturbulence used was as high as 90% of the mean mass flow rate to match with the experimental conditions. Another case with a low-level fluctuation on the order of 1% at the injection surface was also studied. The inflow boundary conditions can be summarized as follows:

$$\rho^r \tilde{v}_w^r = \varepsilon_p \bar{\dot{m}}_w (2\Re - 1) \tag{21}$$

$$\tilde{u}^r = 0 \tag{22}$$

Note that white noise is introduced in both temporal and spatial distributions of $\bar{m}_w$. The momentum equation in the vertical direction is then solved to obtain the pressure. At the injection surface, the effect of kinetic energy variation on the total specific energy $\tilde{e}^r$ is minimal. Thus, the temperature and pressure fluctuations at the wall are not significant.

At the head end of the motor, the gradients of axial pressure and vertical velocity are set to zero, along with the adiabatic condition. Application of the slip condition at the head end is necessary to avoid a numerically induced recirculating flow at the injection surface.[15,28] Symmetry conditions are applied along the centerline of the motor. The supersonic outflow requires no boundary conditions, according to the method of characteristics. The flow variables at the exit are extrapolated from those within the computational domain.

III. Numerical Method and Error Analysis

An accurate numerical scheme is essential for resolving various timescales and length scales of turbulent motions. The issue of a priori estimation of computational errors in turbulence simulations has recently been addressed by several researchers.[29,30] Ghosal[29] analyzed the truncation errors of the various terms in finite difference equations and compared the contributions of the errors at a given time with the exact terms for incompressible flow equations. A model turbulence spectrum was employed to facilitate the comparison. Results indicated that for finite difference methods the errors created by approximating the convection terms generally dominate errors introduced by other terms in the governing equation. These convection terms are important in any turbulence computation at large Reynolds numbers because they represent the dominance of inertial force over viscous force. Fabignon et al.[30] and Beddini et al.[31] extended the von Neumann stability analysis (see Refs. 32 and 33) to assess the importance of the errors associated with convection terms by introducing a reference spectrum obtained from homogeneous, isotropic turbulence theory. This energy spectrum was convected in accordance with the amplification factor of the numerical scheme and then compared with the initial spectrum after one large-eddy lifetime. An estimation of the numerical errors of nonlinear convection terms was made. The fourth-order Runge–Kutta scheme with the sixth-order Padĕ's compact differencing for spatial descretization (RK4-6CP) was shown to resolve the turbulence energy spectrum in the inertial range for a wide range of Mach numbers. A significant reduction in computational time, as compared with RK4-6CP, can be achieved by means of an alternative Runge–Kutta scheme presented by Jameson,[34] which is fourth-order accurate in time and uses fourth-order central differencing in space (RK4-4C). It was shown by Beddini et al.[31] that the RK4-4C scheme resolves the energy spectrum with accuracy comparable to that of the sixth-order Padĕ scheme over a wide range of Mach numbers. The compromise between computational time and spatial accuracy led to the choice of Jameson's method for use in the present study.

Following the analyses of Fabignon et al.[30] and Beddini et al.,[31] the effect of computational errors on SGS modeling is investigated herein based on the Smagorinsky subgrid eddy-viscosity model. The work extends the previous effort to study the effects of SGS model and artificial dissipation, introduced in central-difference schemes for numerical stabilization, on the turbulence energy spectrum. A thorough investigation is carried out for the RK4-4C method. The transport equation for the energy spectrum function $E(k,t)$ for homogeneous turbulent flows can be expressed as[31]

$$\frac{\partial}{\partial t}E(k,t) + (\bar{u}_k)_{AB}\left[\frac{\partial}{\partial x_k}E(k,t)\right]_{AB} = T(k,t) - D(k,t) - P(k,t) \tag{23}$$

where $T(k,t)$ represents the energy transfer between wave numbers, $D(k,t)$ the viscous dissipation, and $P(k,t)$ the production term. A and B represent the points in the flowfield for two-point correlation. For stationary flows, the first term on the left-hand side is zero. Retention of the convective terms for spectral transport enables the present estimation of convection errors. Convection of the energy spectrum is assumed to take place at a constant mean velocity $\bar{u}_k$. The main objective of this work is to utilize a representative turbulence spectrum, obtained from the model of the transfer, dissipation, and production terms in the preceding equation, to allow for the estimation of the effectiveness of a numerical scheme. The initial kinetic energy spectrum is introduced using Tennekes and Lumley's analysis.[35] It models the production-dominated part of the spectrum at low wave numbers, representing large, energy-carrying structures, and provides the classical $k^{-5/3}$ power law in the inertial subrange, representing equilibrium turbulence. The initial dimensionless spectrum of turbulent energy is given as[31]

$$E(k,0) = \alpha(\delta Re_c)^{-\frac{5}{4}}(k\eta)^{-\frac{5}{3}}\exp\left[-1.5\pi\beta\sqrt{\alpha}(\delta Re_c)^{-1}(k\eta)^{-\frac{4}{3}}\right] \tag{24}$$

where α is the Kolmogorov constant and η the Kolmogorov length scale. Experimental data show that α and β are 1.5 and 0.3, respectively.[30,31] An order-of-magnitude estimate relates the turbulent Reynolds number ($Re_t = q\ell/\nu$) and the Reynolds number at the centerline of the motor ($Re_c = \bar{u}_c h/\nu$),

$$Re_t \approx \delta Re_c \tag{25}$$

where $\sqrt{\delta} \approx q/\bar{u}_c \approx \ell/h$. In the preceding expressions, ℓ is the integral length scale, h the channel half-height, $\bar{u}_c$ the centerline velocity, and q the rms of fluctuating velocity.

Convection of the initial energy spectrum depends on the numerical scheme and takes the form

$$E(k,\tau) = |G_{k,u}|^{I_\tau} E(k,0) \tag{26}$$

where $G_{k,u}$ is the amplification factor obtained from the eigenvalue u of the numerical scheme. I_τ is the number of time steps required to reach one eddy lifetime τ, which depends on the grid size and the Courant–Friedrichs–Lewy (CLF) number σ.

$$I_\tau = \delta^{\frac{1}{4}}[(M+1)/\xi M\sigma]Re_c^{\frac{3}{4}} \tag{27}$$

where ξ is the grid parameter ($\Delta x/\eta$). This approach provides a basis for selection of grid size for the LES, which requires the cutoff wave number to be in the inertial range of the energy spectrum.

Figure 2 shows the spectrum for the RK4-4C scheme for various CFL numbers after one eddy lifetime, at a representative motor condition of $Re_c = 3\times10^5$ and $M_c = 0.5$. No artificial dissipation is considered in this analysis, that is, $\varepsilon_v = 0$. The grid parameter ξ of unity implies that the entire range of turbulence scale, up to the Kolmogorov length scale, is modeled as in a DNS. Here, ξ usually varies between 10 and 50 for typical LES and is approximately 15 in the present computation. Decrease in ξ shifts the cutoff point toward the DNS value. Here $\xi = 25$ is used to illustrate the range of scale resolved in LES as compared with DNS. The numerical scheme becomes neutrally stable at the maximum wave number, and the spectrum rises to the cutoff point, as shown in Fig. 2. Increase in the CFL number reduces the resolution of the energy spectrum because of the reduction in the cutoff wave number. Because the computational time is inversely proportional to the CFL number, a CFL number of 0.5 is found to be a good compromise between accuracy and computational time.

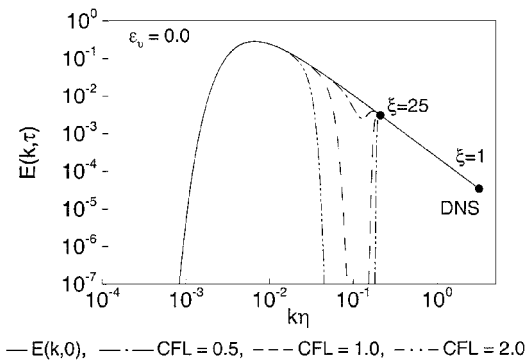

Fig. 2 Dimensionless turbulent energy spectrum of RK4-4C scheme at different CFL numbers with $\xi = 25$.

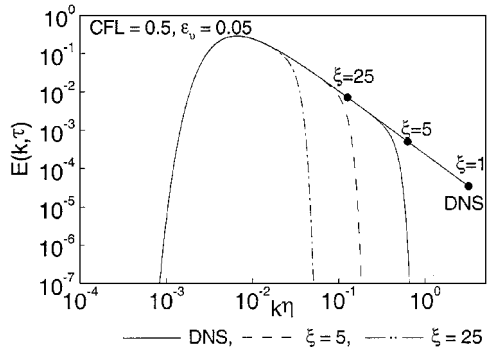

Fig. 3 Dimensionless turbulent energy spectrum of RK4-4C scheme at different grid parameters with CFL = 0.5.

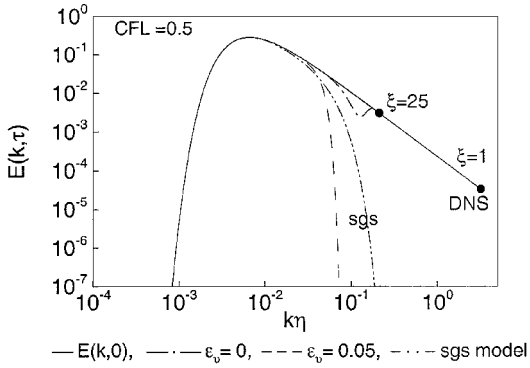

Fig. 4 Effect of artificial dissipation and SGS model on dimensionless turbulent energy spectrum of RK4-4C scheme with $\xi = 25$.

Artificial dissipation is essential to reduce the amplification factor and stabilize numerical schemes based on central differencing at high wave numbers. Figure 3 shows the effect of the grid parameter and artificial dissipation in resolving the energy spectrum. With the addition of sixth-order artificial dissipation terms, the neutrally stable point at the peak wave number is eliminated. As the grid parameter ξ increases, the grid resolution decreases, and hence, the effective artificial dissipation increases. The energy spectra deviate earlier from the initial spectrum with increase in the grid size. Figure 4 shows the effect of the sixth-order artificial dissipation and Smagorinsky's SGS model on convection of the energy spectrum. The eddy-viscosity hypothesis gives an estimate of the energy spectrum evolution as[36]

$$E(k,\tau) = E(k,0)\exp\left[-2(k\eta)^2\sqrt{\delta Re_c}(1+\nu_T/\nu)\right] \tag{28}$$

where the eddy viscosity ν_T is obtained from the SGS model as

$$\nu_T/\nu = 4.11c_S^2\left(\sqrt{\alpha}\beta\right)^{\frac{1}{4}}\xi^{\frac{4}{3}} \tag{29}$$

The artificial and SGS-dissipations are of the same order in the present case, as evidenced in Fig. 4. Ragab and Sheen[37] indicate that the dissipation mechanism in a three-dimensional turbulent flow is very different from the artificial dissipation because of the vortex stretching and rolling phenomena. Liou et al.[20] showed in their two-dimensional simulation of injection-driven flows that SGS stresses have little effect on the turbulence characteristics, and the artificial dissipation introduced by the numerical scheme may serve as an SGS model. The Smagorinsky SGS model is purely dissipative, and hence, numerical dissipation may serve the same purpose under certain flow configurations.

Because of the enormous computational effort required, especially for problems involving forced acoustic oscillations, as discussed in Ref. 23, only two-dimensional calculations were performed in the work described herein. The analysis, in spite of the lack of vortex-stretching mechanism, has been shown to be more accurate than conventional models based on second-order turbulence closure schemes and allows for a systematic investigation of the oscillatory flowfields in a rocket motor. Results were corroborated in a subsequent study using full three-dimensional large-eddy simulations,[22,28] indicating that the two-dimensional computations can capture the salient features of the mean and turbulent flowfields.

IV. Flow Evolution

The analysis described is used first to study the flow development in a simulated nozzleless rocket motor, as shown schematically in Fig. 1. The chamber is two dimensional and measures 48 cm in length and 2 cm in height. The nozzle at the exit is 3.2 cm long with a divergence angle of 15 deg. The configuration and flow parameters studied are based on the experiment of Traineau et al.[11] Air is injected through the porous surface at a total temperature of 260 K and a total pressure of 3.142 atm. The mean injection mass flux is kept constant at $\bar{m}_w = 13$ kg/m^{2}s, giving an injection velocity of 3.1 m/s. The numerical calculation is initialized with the analytical velocity profile for an inviscid incompressible flow with surface mass injection,[8,9]

$$\tilde{u}^r \big/ \tilde{u}_c^r = \cos[(\pi/2)(y/h)] \tag{30}$$

White noise is introduced in the inflow mass flux to perturb the mean flow for turbulence transition. The magnitude of perturbation is 90% of the mean quantity $\bar{m}_w$. Such a high level of turbulence intensity at the surface is employed to facilitate comparison with experimental conditions as indicated by Traineau et al.[11] The effect of low levels of pseudoturbulence on turbulence transition and intensity is also investigated by simulating the flowfield with $\dot{m}'_w = 0.01\bar{m}_w$. These perturbations, however, are transformed into the combined effect of oscillations in density and vertical injection velocity and do not lead to suction at the porous surface. The computational domain consists of 640×100 cells in the axial and vertical directions, respectively. A uniform grid is used in the x direction, whereas the grid is stretched toward the surface in the y direction with the smallest grid size on the order of 50 μm. The grid size based on the grid parameter ξ is on the order of 15 and is sufficient to resolve the energy spectrum in the inertial subrange, as shown later. The CFL number used is 0.5, and the time step is fixed at 5×10^{-8} s for time-accurate simulations. An outbreak of turbulence occurs at 4–5 ms of the physical time starting from the flow initialization based on Eq. (30). Stationary oscillations are obtained during 8–17 ms, and the mean flow properties are evaluated in this time zone. Accordingly, the run time for these simulations was around 200–250 CPU hours on a Pentium II machine as the data was collected over 4–5 flow-through times to obtain statistically meaningful turbulence properties. The short run time for two-dimensional simulations provides an opportunity to extend this work to study the intriguing phenomenon of acoustically induced turbulence. Several computations with periodic excitations at different amplitudes and frequencies were performed in Ref. 23 to investigate the interactions among the mean, periodic, and turbulent flowfields.

Instantaneous Flowfield

Figure 5 shows the temporal evolution of the vorticity field. To facilitate discussion, only the lower half of the chamber is presented, where $y/h = 1$ corresponds to the injection surface. Vorticity is produced at the porous surface because of the no-slip condition.[38]

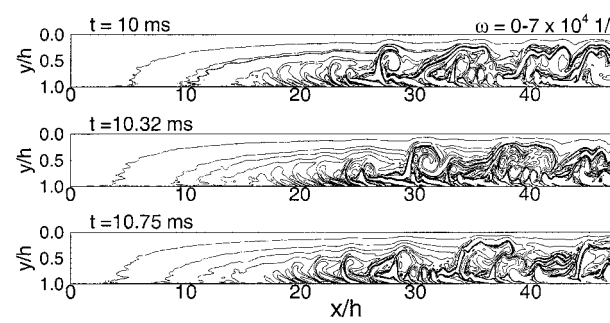

Fig. 5 Temporal evolution of vorticity field.

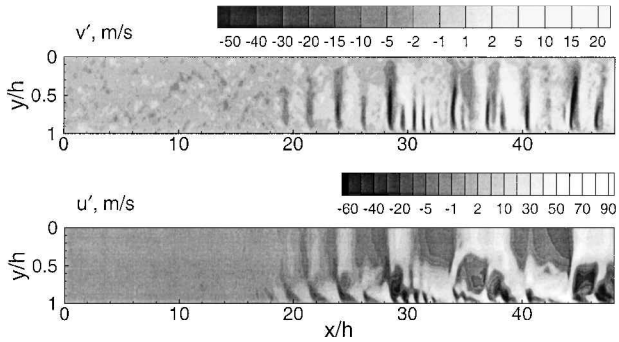

Fig. 6 Snapshots of fluctuating velocity fields; $t = 10.32$ ms.

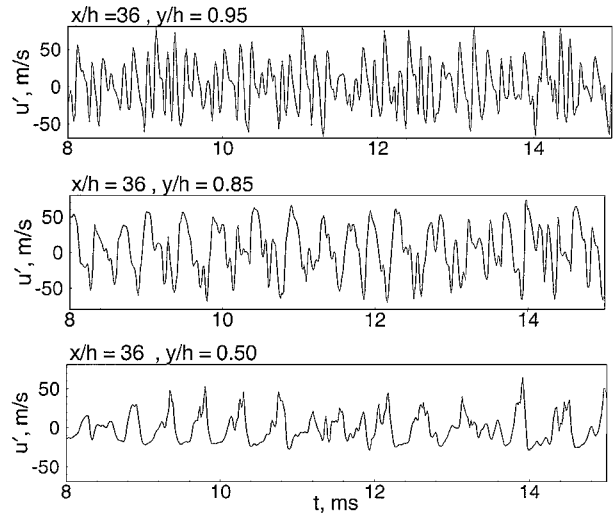

Fig. 7 Temporal evolution of axial velocity fluctuations at various vertical locations in turbulent regime; $x/h = 36$.

At the injection surface,

$$\omega = \left(\frac{\partial \tilde{v}'}{\partial x} - \frac{\partial \tilde{u}'}{\partial y} \right)_w \tag{31}$$

As the flow accelerates in the axial direction, pressure and density decrease while the injection velocity v_w increases to keep the mass inflow rate $\dot{m}_w$ constant. The axial variation of v_w, however, is not significant, and the vorticity ω is dictated by the vertical gradient of the axial velocity component. As the flow undergoes transition to turbulence, this gradient increases rapidly, giving a higher level of vorticity in the turbulent regime. Near the head end, turbulent fluctuations appear to be small, and the flow is mostly laminar. Transition to turbulence occurs around $x/h = 20$–25, and the flow becomes highly turbulent farther downstream. Vorticity is rapidly convected away from the surface in this inertia-dominated flow, as evidenced by the presence of large energy-carrying structures. Figure 6 shows the instantaneous contours of fluctuating vertical and axial velocities at $t = 10.32$ ms, obtained by subtracting the long-time-averaged flowfield from the instantaneous solution. The fluctuation levels are small in the upstream laminar regime and grow as the large-scale vortical structures evolve in the turbulent regime. The random noise introduced at the injection surface of the chamber grows into a broadband spectrum with the hydrodynamically unstable modes displaying large-scale oscillations. The fluctuations in vertical velocity at the porous wall are transferred into the axial velocity oscillations and are convected downstream by the mean flowfield. Figure 7 shows the time variation of the fluctuating axial velocity at various vertical locations in the turbulent regime. The magnitude of the axial velocity fluctuation decreases away from the injection surface, indicating a decrease in turbulence intensity toward the centerline. The signal is collected over a time span of 8 ms to obtain statistically meaningful flow properties.

The present two-dimensional computation lacks the vortex-stretching phenomenon responsible for the transfer of energy from the large to the small scales through the energy cascade mechanism and, consequently, leads to lower dissipation and production rates. Nevertheless, it provides much useful insight into flow development, which was not previously available using second-order turbulence closure schemes.

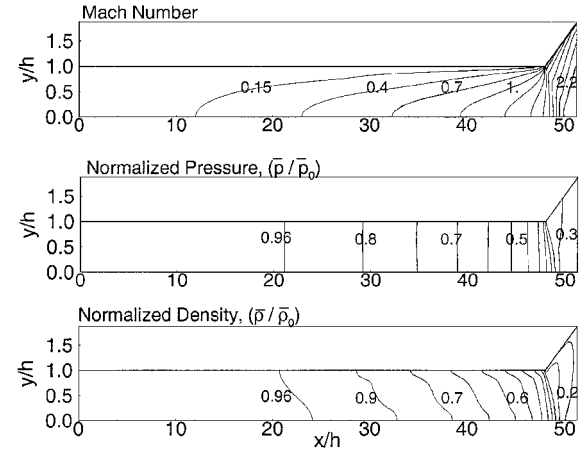

Fig. 8 Contour plots of mean Mach number, pressure, and density.

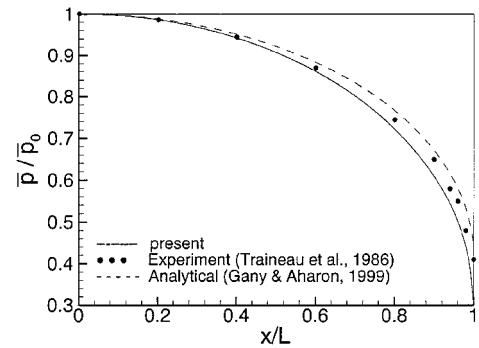

Fig. 9 Axial variation of mean chamber pressure.

Mean Flow Properties

Figure 8 shows the contour plots of the time-averaged Mach number, pressure, and density fields. The exit Mach number of 2.2 agrees well with the analytical value for an isentropic flow through a divergent nozzle with known area ratio and given stagnation pressure and temperature upstream. The pressure field is basically one dimensional, due to the small injection Mach number, with increasing gradient toward the throat area. Figure 9 shows the axial variation of the mean pressure compared with experimental data. Also indicated is the variation of pressure obtained by Gany and Aharon[39] using a one-dimensional analysis of frictionless flow with mass injection. For uniform injection at constant mass flow rate, the variation in pressure is given as

$$\bar{p}/\bar{p}_0 = \frac{1 + \gamma\sqrt{1 - (x/L)^2}}{1 + \gamma} \tag{32}$$

where $\bar{p}_0$ is the mean chamber pressure at the head end, L the length of the porous chamber, x the axial location from the head end, and γ the ratio of the specific heats. Figures 10 and 11 show the axial and vertical variations of the mean axial velocity, along with the analytical solution for an incompressible laminar flow.[8,9] Good agreement with the experimental data of Traineau et al.[11] is obtained. The flow is predominantly incompressible and laminar in the upstream region of the chamber. Deviation from the incompressible-flow solution starts between $x/h = 20$ and 30, due to the increasing Mach number and, hence, the compressibility effect. In the present study, the injection mass flux is kept constant. As a result of rapidly decreasing density toward the throat area, the local flow velocity increases and leads to differences between this velocity profile and its incompressible-flow counterpart. The enhanced momentum transfer due to turbulence also plays an important role.

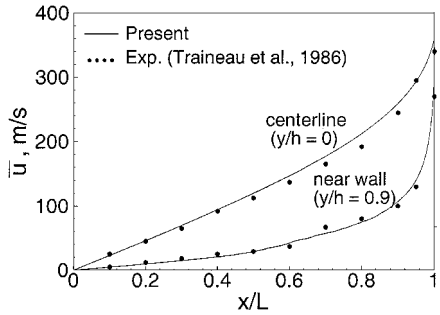

Fig. 10 Variations of mean axial velocity in axial direction.

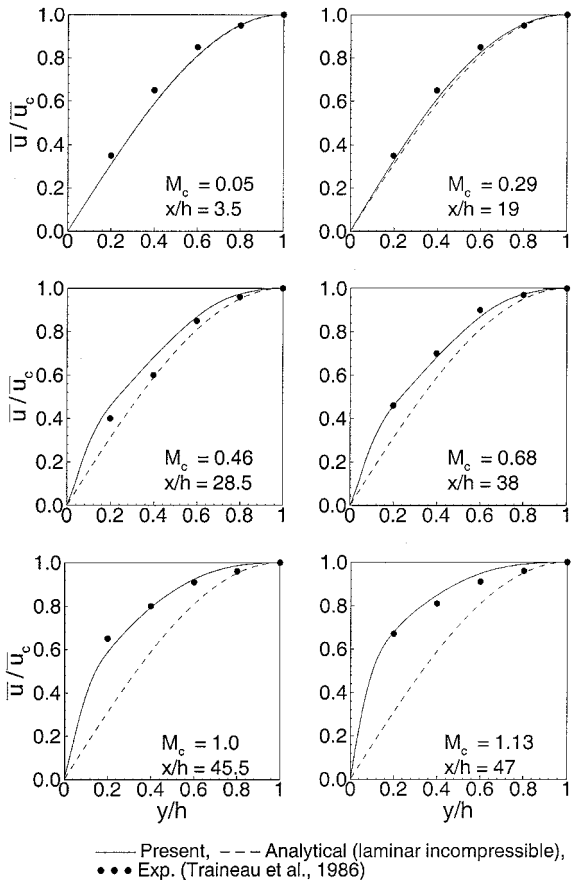

Fig. 11 Variations of normalized mean axial velocities in vertical direction.

The transition of the mean velocity profile can be characterized in terms of the momentum flux coefficient β, as proposed by Huesmann and Eckert[40]:

$$\beta = \frac{\int_0^h \bar{\rho}\bar{u}^2\,\mathrm{d}y}{\bar{\rho}_b \bar{u}_b^2 h} \tag{33}$$

where the subscript b denotes the bulk mean quantity, obtained by averaging the corresponding flow property over a given cross section of the chamber. Figure 12 compares the calculated β with experimental data.[11] The momentum flux coefficient has a constant value of 1.234 for laminar incompressible flow and can be obtained by substituting Eq. (30) into Eq. (33). The decreasing density and increasing injection velocity toward the nozzle alter the vertical variation of the axial velocity and, consequently, cause an accelerated decrease in the β value in the downstream region. The experimental value of β at the head end is 1.16, instead of 1.234 as predicted by laminar flow theory, because of the high level of turbulence at the porous wall generated in the experiments.[11] The agreement of the calculated β in the upstream region with laminar-flow theory implies uncertainties in the experimental measurements. Both the numerical and experimental data show faster variation between $x/h = 20$ and

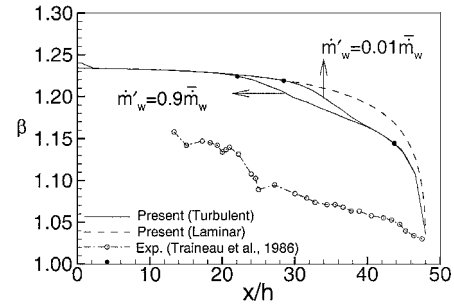

Fig. 12 Variations of momentum flux coefficients in axial direction at different pseudoturbulence levels.

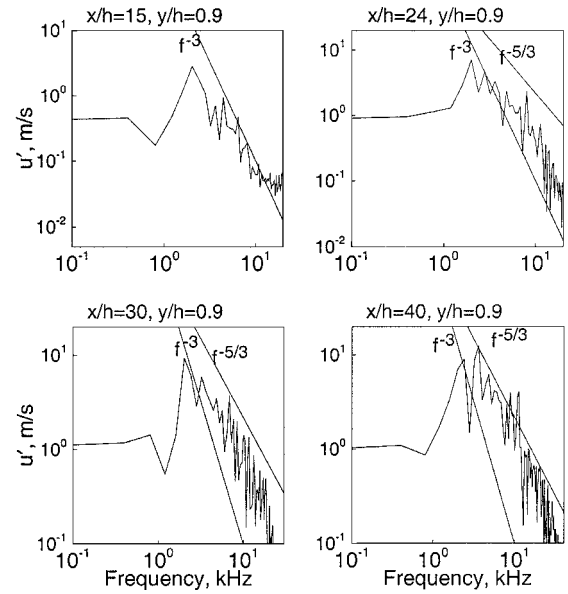

Fig. 13 Turbulent energy spectra of axial velocity fluctuations at various axial locations.

30 in the turbulent regime. These results are qualitatively similar to those obtained by Beddini[10] for an axisymmetric duct with a low level of pseudoturbulence at the porous wall.

The effect of surface-generated turbulence on the flow development is also studied. For a high level of wall turbulence, that is, $\dot{m}'_w = 0.9\bar{\dot{m}}_w$, transition of the mean velocity profile occurs in the upstream of the motor ($x/h = 20$). The transition point shifts downstream ($x/h = 30$) with a lower level of pseudoturbulence, that is, $\dot{m}'_w = 0.01\bar{\dot{m}}_w$, indicating the influence of turbulence on the mean velocity field. Farther downstream ($x/h > 42$), the flowfield is dominated by compressibility effects, and the variation of β closely follows that predicted by laminar compressible-flow theory.

Transport Properties

To make use of the equilibrium hypothesis generally employed in SGS models for estimating the effect of unresolved scales on large-scale structures, the cutoff wave number for turbulence computation should lie in the inertial subrange of the turbulence energy spectrum. This is verified from the energy spectra of the axial velocity fluctuation at various locations, as shown in Fig. 13. The standard $\frac{5}{3}$ law of energy spectrum based on the Kolmogorov–Obukhov theory is not observed in the present two-dimensional simulation. Lesieur et al.[41] and Lesieur[42] indicate in their two-dimensional computation of a temporal mixing layer that the exponent of the wave number in the inertial subrange of the turbulence energy spectrum is close to −4. Gilbert[43] proposed that the kinetic energy spectrum can be obtained from spiral vortex distributions within the coherent vortices and should follow the $f^{-11/3}$ law, where f is frequency. Figure 13 indicates that the spectrum develops as the flowfield undergoes transition from laminar to turbulence in the midsection of the motor. The inertial subrange lies between f^{-3} and f^{-4} variations. The

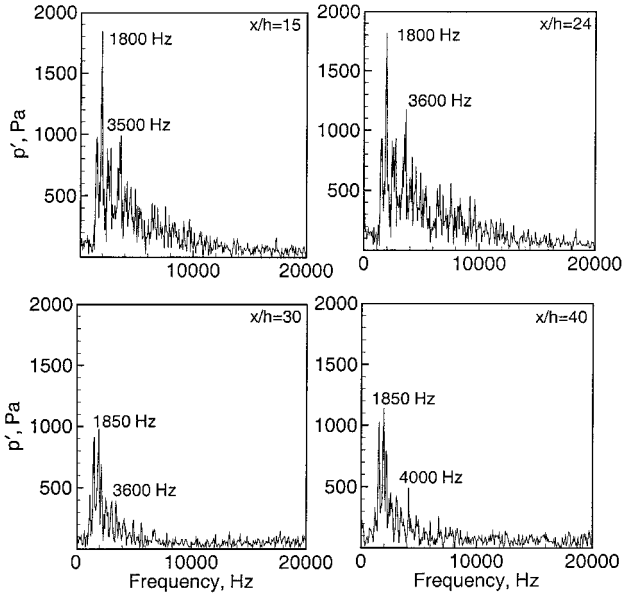

Fig. 14 Power spectral densities of pressure fluctuations at various axial locations; $y/h = 0.9$.

result ensures that the energy spectrum is well captured in the present computation throughout the chamber, which further confirms the adequacy of the computational grid.

Figure 14 shows the power spectral densities of pressure fluctuations at various axial locations. The peak magnitude of pressure fluctuation is around 1% of the mean chamber pressure at the head end. The amplitude of pressure oscillation is found to decrease in the axial direction, mainly due to the decrease in mean pressure as the flow accelerates toward the exit. The fluctuations in pressure may be correlated with the oscillatory vorticity. Low-pressure regions correspond to concentrated vortical structures and highly rotational flow. The oscillations are convected downstream without any reflection into the computational domain because of the supersonic outflow in the divergent nozzle. The peaks in pressure fluctuations at 1800 and 3500 Hz may represent the vortex shedding from the injection surface due to hydrodynamic instability. Recently, Casalis et al.[44] and Ugurtas et al.[45] conducted linear stability analysis and experimental measurements to investigate the stability and acoustic resonance of internal flows in rocket motors. Their analytical approach can be applied to obtain the amplitudes of velocity and pressure fluctuations over the broad spectrum of turbulent motions. The power density spectra of the velocity and pressure fluctuations obtained from present simulations are in qualitative agreement with their stability analysis. The dominant frequency of vortex shedding can be characterized by the Strouhal number $Sr = fh/v_w$. The present study indicates that Strouhal number Sr is around 6, based on the frequency of 1800 Hz. In an effort to investigate the vortex-shedding phenomenon in rocket motors, Avalon et al.[46] also predicted a similar range of Strouhal number for different injection velocities and chamber configurations. Their study indicated that, under the absence of acoustic resonance, the vortex shedding is driven by hydrodynamic instability of the flow. To obtain better understanding of this phenomenon, the described flowfield may be excited at different eigenmodes of the chamber to study the coupling between acoustic waves and vortex shedding. This has been performed in a systematic way in Ref. 23.

Figure 15 shows the vertical variations of turbulence intensity $[I = \sqrt{(u'^2 + v'^2)}]$ and Reynolds stress $(\overline{u'v'})$ at various axial locations. The measured turbulence intensity and Reynolds stress,[11] as well as turbulent flow properties obtained from a three-dimensional LES computation,[22,28] are included for comparison. These three-dimensional simulations were performed on a fine grid with $680 \times 200 \times 50$ numerical cells. The peak in the turbulence intensity increases rapidly and shifts toward the porous wall farther downstream. Because the mass influx is kept constant in the present study, the density decreases and injection velocity increases as the

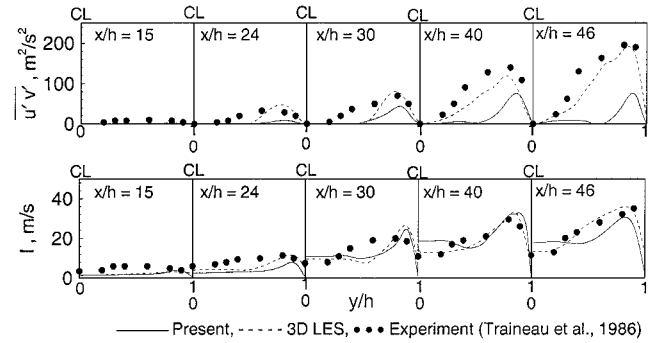

Fig. 15 Variations of Reynolds stress and turbulence intensity in vertical direction at various axial locations.

flow accelerates toward the exit. The increasing injection velocity tends to reduce the wall-damping effect, and therefore, little change in the vertical location of turbulence intensity peak occurs beyond $x/h = 35$. The internal flowfield is dominated by the strain rates in the axial direction, causing higher intensity in the axial component. The underprediction of the Reynolds stress may be attributed to the lack of vortex-stretching mechanisms in the present two-dimensional simulation. The turbulent energy is transferred from large energy-carrying eddies to smaller scales through the energy cascade and is finally dissipated at the molecular level through vortex stretching. The production mechanism in real turbulence is different from that in a two-dimensional simulation because of the additional spanwise direction. The present approach represents an improvement, however, compared with the conventional two-equation models, which do not predict the Reynolds stress and overpredict the turbulence intensity level.[14]

Summary of Internal Flow Development

The overall flow development in the chamber can be characterized by three distinct regimes: laminar, transitional, and fully turbulent flows, as shown schematically in Fig. 16. Near the head end, the flow is laminar, and its velocity profiles can be determined by laminar similarity theory.[8,9] The hydrodynamic instability then renders the flow unstable, and turbulence begins to occur in the downstream region (point A). Unlike channel flows without surface injection, the outbreak of turbulence takes place away from the wall, with the region of intensive turbulence production shifting toward the wall as the flow accelerates in the downstream region. Within the initial transition regime, the mean velocity profiles still correspond to the form predicted by laminar similarity theory because of the predominance of the pressure gradient over the viscous stress. As the flow develops further, a strong turbulent flow regime is observed. The deviation of the mean velocity profiles from those predicted by incompressible-laminar-flow theory becomes significant, due to the combined effect of turbulence and fluid compressibility.

The mean flowfield is basically obtained by balance between the axial pressure gradient and interia forces. Mass injection leads to a decrease in the wall shear stress. The variation of the mean pressure in the axial direction is predominantly governed by a simplified one-dimensional correlation given by Eq. (32). The rapid decrease in pressure toward the nozzle accelerates the flow from zero at the head end to supersonic flow in the divergent section of the nozzle. Although the entire flowfield is driven by the mass injection through the porous wall, the characteristics of each flow regime are dominated by different physical mechanisms. To facilitate discussion, three key parameters characterizing the flow development are defined here: the injection Reynolds number $Re_w \equiv \bar{v}_w h/\nu$, the mean-flow Reynolds number $Re_m \equiv \bar{u}_b h/\nu$, and the momentum flux coefficient β defined in Eq. (33). The laminar-flow regime reaches from the head end to about $x/h = 20$. The turbulence intensity is extremely small, and the velocity profiles can be described by laminar-flow theory. An analytical study conducted by Hu[47] indicates that, for the injection Reynolds numbers Re_w greater than 500, the velocity profiles are almost identical to the prediction based on an inviscid rotational-flow analysis, Eq. (30). Viscous stress, however, becomes important for Reynolds number Re_w less than 100 and changes the velocity

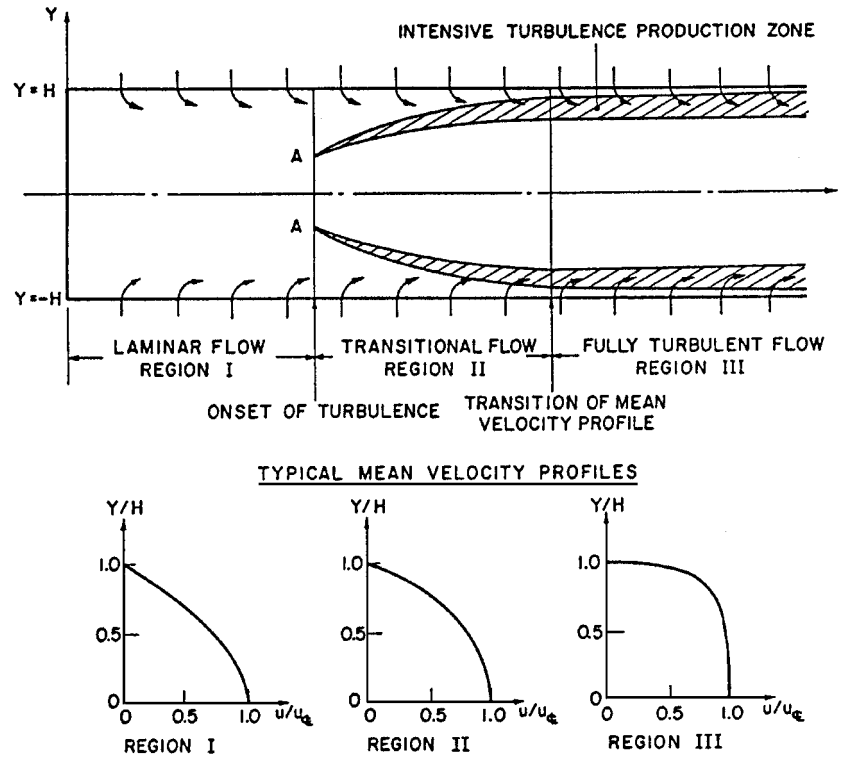

Fig. 16 Schematic diagram of flow development in porous chamber with surface mass injection.

profiles significantly as compared to their inviscid counterparts. This observation is consistent with the experimental findings of Dunlap et al.[48] For high injection Reynolds numbers, the flow is mainly driven by the pressure gradient arising from the mass injection; the viscous shear stress plays a much less important role in determining the flow development. Because the injection Reynolds number near the head end is about 15×10^3 in the present case, the calculated velocity agrees closely with the cosine profile. A similar observation is made for the distribution of the vertical velocity, which can be predicted by the following expression:

$$\tilde{v}^r \Big/ \tilde{v}^r_w = \sin[(\pi/2)(y/h)] \tag{34}$$

The second regime is characterized by the onset of turbulence. When the fluid particle moves downstream, the local velocity and Reynolds number increase and eventually reach a point at which turbulent fluctuations occur. The classical hydrodynamic instability analysis of the Poiseulle flow cannot accurately predict the laminar-to-turbulence transition in a porous duct with surface transpiration. Varapaev and Yagodkin[49] found that the effect of the vertical velocity component must be taken into account in predicting the critical Reynolds number Re^* for the onset of turbulent oscillation. For a small injection Reynolds number, a substantial reduction of Reynolds number Re^* from its counterpart for an impermeable pipe flow is observed, due to the destabilizing effect of the transverse velocity component. For Reynolds number Re_w greater than 300, however, the critical Reynolds number increases linearly with Reynolds number Re_w, due to the stabilizing effect of the resultant favorable pressure gradient. Figure 15 indicates that the turbulent kinetic energy remains at a very low level in the head end region up to $x/h = 20$ and increases rapidly afterward. The mean velocity profile only changes slightly, as shown in the transitional region, that is, $20 < x/h < 25$, in Figs. 11 and 12. Casalis et al.[44] also elucidated through their linear stability analysis that the injection velocity and the channel height play important roles in determining the hydrodynamic stability of injection-driven flows in porous chambers.

As the flow develops farther downstream, the velocity profile transits into the shape of a fully developed turbulent pipe flow with surface transpiration. The axial velocity gradient becomes much steeper near the wall, but smoother in the core region. The value of the momentum flux coefficient β decreases down to 1.04 at the chamber exit. Note that, in addition to the turbulence effect, fluid compressibility may exert more significant influence on the variation of the velocity profile due to the large density gradient in the downstream region.

V. Conclusions

A comprehensive numerical study of the flow development in a porous chamber with surface mass injection has been performed by means of an LES technique. The effect of turbulence and fluid compressibility on the mean flow structure was examined in depth. The flowfield is characterized with three distinct regimes: laminar, transitional, and fully developed turbulent flows. The effect of mass injection is primarily to decrease the wall shear stresses. The flowfield is governed by the balance between pressure gradient and inertia forces, as opposed to the viscous stresses and pressure gradient as in channel flows without injection. In spite of its lack of vortex-stretching phenomenon, however, the present two-dimensional simulation captures the salient features of the flowfield and provides much useful insight into the flow development, which was not previously available using second-order turbulence closure schemes.

References

[1] Mickley, H. A., Ross, R. C., Squyers, A. L., and Stewart, A. A., "Heat, Mass and Momentum Transfer for Flow over a Flat Plate With Blowing or Suction," NACA TN 3208, 1954.

[2] Simpson, R. L., Moffat, R. J., and Kays, W. M., "The Turbulent Boundary Layer on a Porous Plate: Experimental Skin Friction with Variable Injection and Suction," *International Journal of Heat and Mass Transfer*, Vol. 12, 1969, pp. 771–789.

[3] Julien, H. L., Kays, W. M., and Moffat, R. J., "Experimental Hydrodynamics of the Accelerated Turbulent Boundary Layer With and Without Mass Injection," *Journal of Heat Transfer*, Vol. 93, 1972, pp. 373–379.

[4] Kays, W. M., "Heat Transfer to the Transpired Boundary Layer," *International Journal of Heat and Mass Transfer*, Vol. 15, 1974, pp. 1023–1044.

[5] Kays, W. M., and Crawford, M. E., *Convective Heat and Mass Transfer*, 2nd ed., McGraw–Hill, New York, 1980.

[6] Piomelli, U., Moin, P., and Ferziger, J., "Large Eddy Simulation of Flow in a Transpired Channel," *Journal of Thermophysics*, Vol. 5, No. 1, 1991, pp. 124–128.

[7] Sumitani, Y., and Kasagi, N., "Direct Numerical Simulation of Turbulent Transport with Uniform Wall Injection and Suction," *AIAA Journal*, Vol. 33, No. 7, 1995, pp. 1220–1228.

[8]Taylor, G. I., "Fluid Flow Regions Bounded by Porous Surfaces," *Proceedings of the Royal Society of London*, Series 234A, Vol. 11199, 1956, pp. 456–475.

[9]Culick, F. E. C., "Rotational Axisymmetric Mean Flow and Damping of Acoustic Waves in Solid Propellant Rocket Motors," *AIAA Journal*, Vol. 4, 1966, pp. 1462–1464.

[10]Beddini, R. A., "Injection Induced Flows in Porous-Walled Ducts," *AIAA Journal*, Vol. 24, No. 11, 1986, pp. 1766–1773.

[11]Traineau, J. C., Hervat, P., and Kuentzmann, P., "Cold-Flow Simulation of a Two-Dimensional Nozzleless Solid-Rocket Motor," AIAA Paper 86-1447, 1986.

[12]Balakrishnan, G., Linan, A., and Williams, F. A., "Rotational Inviscid Flow in Laterally Burning Solid-Propellant Rocket Motors," *Journal of Propulsion and Power*, Vol. 8, No. 6, 1992, pp. 1167–1176.

[13]Dunlap, R., Blackner, A. M., Waugh, R. C., Brown, R. S., and Willoughby, P. G., "Internal Flowfield Studies in a Simulated Cylindrical Port Rocket Chamber," *Journal of Propulsion and Power,* Vol. 8, No. 6, 1992, pp. 1167–1176.

[14]Sabnis, J. S., Madabhushi, R. K., Gibeling, H. J., and McDonald, H., "On the Use of $k-\varepsilon$ Turbulence Model for Computation of Solid Rocket Internal Flows," AIAA Paper 89-2558, 1989.

[15]Tseng, I. S., "Numerical Simulation of Velocity-Coupled Combustion Response of Solid Rocket Propellants," Ph.D. Dissertation, Dept. of Mechanical Engineering, Pennsylvania State Univ., University Park, PA, 1992.

[16]Nicoud, F., Poinsot, T. J., and Minh, H. H., "Direct Numerical Simulation of a Turbulent Flow with Massive Uniform Injection," *10th Symposium on Turbulent Shear Flows*, Vol. 3, No. 29, 1995, pp. 13–18.

[17]Ciucci, A., Iaccarino, G., Moser, R., Najjar, F., and Durbin, P., "Simulation of Rocket Motor Internal Flows with Turbulent Mass Injection," *Proceedings of the Summer Program*, Center for Turbulence Research, Stanford Univ., Stanford, CA, 1998, pp. 245–266.

[18]Lupoglazoff, N., and Vuillot, F., "Parietal Vortex Shedding as a Cause of Instability for Long Solid Propellant Motors—Numerical Simulations and Comparisons with Firing Tests," AIAA Paper 96-0761, 1996.

[19]Liou, T. M., and Lien, W. H., "Numerical Simulations of Injection-Driven Flows in a Two-Dimensional Nozzleless Solid-Rocket Motor," *Journal of Propulsion and Power*, Vol. 11, No. 4, 1995, pp. 600–606.

[20]Liou, T. M., Lien, W. Y., and Hwang, P. W., "Transition Characteristics of Flowfield in a Simulated Solid-Rocket Motor," *Journal of Propulsion and Power*, Vol. 14, No. 3, 1998, pp. 282–289.

[21]Apte, S.V., and Yang, V., "Effects of Acoustic Oscillation on Flow Development in a Simulated Nozzleless Rocket Motor," *Solid Propellant Chemistry, Combustion, and Motor Interior Ballistics*, edited by V. Yang, T. B. Brill, W. Ren, Vol. 185, Progress in Aeronautics and Astronautics, AIAA, Reston, VA, 2000, pp. 791–822.

[22]Apte, S.V., and Yang, V., "Large Eddy Simulation of Internal Flowfield in a Porous Chamber with Surface Mass Injection," *Journal of Fluid Mechanics* (submitted for publication).

[23]Apte, S. V., and Yang, V., "Unsteady Flow Evolution in a Porous Chamber with Surface Mass Injection, Part 2: Acoustic Excitation," *AIAA Journal* (submitted for publication).

[24]Batchelor, G. K., *An Introduction to Fluid Dynamics*, Cambridge Univ. Press, Cambridge, England, U.K., 1967, pp. 131–173.

[25]Erlebacher, G., Hussaini, M. Y., Speziale, C. G., and Zang, T. A., "Toward the Large-Eddy Simulation of Compressible Turbulent Flows," Inst. for Computer Applications in Science and Engineering, *Journal of Fluid Mechanics*, Vol. 238, 1992, pp. 155–185.

[26]Hinze, J. O., *Turbulence*, McGraw–Hill, New York, 1975, pp. 321–357.

[27]Piomelli, U., "Large-Eddy Simulation of Turbulent Flows," Theoretical and Applied Mechanics Rept. 767, Univ. of Illinois, Urbana, IL, 1994.

[28]Apte, S. V., "Unsteady Flow Evolution and Combustion Dynamics of Homogeneous Propellant in a Rocket Motor," Ph.D. Dissertation, Dept. of Mechanical Engineering, Pennsylvania State Univ., University Park, PA, 2000.

[29]Ghosal, S., "An Analysis of Numerical Errors in Large-Eddy Simulations of Turbulence," *Journal of Computational Physics*, Vol. 125, 1996, pp. 187–206.

[30]Fabignon, Y., Beddini, R. A., and Lee., Y, "Analytic Evaluation of Finite Difference Methods for Compressible Direct and Large Eddy Simulations," *Aerospace Science and Technology*, Vol. 6, 1997, pp. 413–423.

[31]Beddini, R. A., Lee, Y., and Fabignon, Y., "Estimation of Convection Errors of Finite Difference Methods for Compressible Turbulence Simulations," Rept. FEDSM97-3116, June 1997.

[32]Anderson, D. A., Tannehill, J. C., and Pletcher, R. H., *Computational Fluid Mechanics and Heat Transfer*, Computational Methods in Mechanics and Thermal Sciences, Hemisphere, New York, 1984, pp. 70–118.

[33]Hirsch, C., *Numerical Computation of Internal and External Flows,* Vol. 1, Wiley, New York, 1992, pp. 238–341.

[34]Jameson, A., "The Evolution of Computational Methods in Aerodynamics," *Journal of Applied Mathematics*, Vol. 50, 1983, pp. 1052–1070.

[35]Tennekes, H., and Lumley, J. L., *A First Course in Turbulence,* MIT Press, Cambridge, MA, 1972, pp. 248–287.

[36]Beddini, R. A., Lee, Y., and Fabignon, Y., "Effects of Convection Errors on Compressible Turbulence Simulations," First Air Force Office of Scientific Research International Conf. on Direct and Large Eddy Simulation, Paper N-16, 1997.

[37]Ragab, S. A., and Sheen, S. C., "Large Eddy Simulation of Mixing Layers," *Large Eddy Simulation of Complex Engineering and Geophysical Flows*, edited by B. Galperin and S. A. Orszag, Cambridge Univ. Press, New York, 1993, pp. 255–285.

[38]Flandro, G. A., "Effects of Vorticity on Rocket Combustion Stability," *Journal of Propulsion and Power*, Vol. 11, No. 4, 1995, pp. 607–625.

[39]Gany, A., and Aharon, I., "Internal Ballistics Considerations of Nozzleless Rocket Motors," *Journal of Propulsion and Power*, Vol. 15, No. 6, 1999, pp. 866–873.

[40]Huesmann, K., and Eckert, E. R. G., "Studies of the Laminar Flow and the Transition to Turbulence in Porous Tubes with Uniform Injection Through the Tube Wall," *Journal of Propulsion and Power,* Vol. 6, No. 6, 1990, pp. 690–705.

[41]Lesieur, M., Staquet, C., Le Roy, P., and Comte, P., "The Mixing Layer in its Coherence Examined from the Point of View of Two-Dimensional Turbulence," *Journal of Fluid Mechanics*, Vol. 192, 1988, pp. 511–534.

[42]Lesieur, M., *Turbulence in Fluids*, 3rd ed., Kluwer Academic, Norwell, MA, 1990, pp. 295–300.

[43]Gilbert, A. D., "Spiral Structures and Spectra in Two-Dimensional Turbulence," *Journal of Fluid Mechanics*, Vol. 193, 1988, pp. 475–498.

[44]Casalis, G., Avalon, G., and Pineau, J.-P., "Spatial Instability of Planar Channel Flow with Fluid Injection Through Porous Walls," *Physics of Fluids*, Vol. 10, No. 10, 1998, pp. 2558–2568.

[45]Ugurtas, B., Avalon, G., Lupoglazoff, N., Vuillot, F., and Casalis, G., "Stability and Acoustic Resonance of Internal Flows Generated by Side Injection," *Solid Propellant Chemistry, Combustion, and Motor Interior Ballistics*, edited by V. Yang, T. B. Brill, and W. Ren, Vol. 185, Progress in Aeronautics and Astronautics, AIAA, Reston, VA, 2000, pp. 823–836.

[46]Avalon, G., Ugurtas, B., Grish, F., and Bresson, A., "Numerical Computations and Visualization Tests of the Flow Inside a Cold Gas Setup: Simulation with Characterization of a Parietal Vortex Shedding," AIAA Paper 2000-3387, 2000.

[47]Hu, T. S., "Flowfield and Heat Transfer in the Entrance Region of a Duct with Closed End and Uniform Injection," M.S. Thesis, Dept. of Mechanical Engineering, Pennsylvania State Univ., University Park, PA, 1990.

[48]Dunlap, R., Blackner, A. M., Waugh, R. C., Brown, R. S., and Willoughby, P. G., "Internal Flow Field Studies in a Simulated Cylindrical Port Rocket Chamber," *Journal of Propulsion and Power,* Vol. 6, No. 6, 1990, pp. 690–704.

[49]Varapaev, V. N., and Yagodkin, V. I., "Flow Stability in a Channel with Porous Walls," *Izvestiya Akademii Nauk SSSR, Mechanika Zhidkosti i Gaza*, Vol. 4, No. 5, 1969, pp. 91–95.

J. P. Gore
Associate Editor